Journal of Materials Science: Materials in Electronics (2018) 29:8785–8792
https://doi.org/10.1007/s10854-018-8895-5

A comparative device performance assesment of CVD grown MoS_2 and WS_2 monolayers

Hüseyin Şar[1] · Ayberk Özden[2] · Buşra Yorulmaz[2] · Cem Sevik[3] · Nihan Kosku Perkgoz[1] · Feridun Ay[1]

Received: 28 December 2017 / Accepted: 9 March 2018 / Published online: 15 March 2018

Abstract

In this study, optical and electronic transport properties of chemical vapor deposition (CVD) grown 2D WS_2 and MoS_2 based transistors and photodetectors are investigated and compared in ambient air by using 2D flakes grown with the same CVD system. To assess the performance variations between these two materials and understand the underlying mechanisms, it is essential to utilize identical growth methods (i.e. using the same CVD system), identical substrate and dielectric materials with the identical device fabrication methods and geometries. Transistor devices fabricated out of these flakes are examined in terms of their field effective mobility, current ON/OFF ratio, and photoresponsivity. Our results show that the MoS_2 based devices have higher mobility and photoresponsivity than the WS_2 based devices. However, the hysteresis curve of WS_2 based transistors is smaller when compared to that of MoS_2 based transistors. The mobilities of MoS_2 and WS_2 are estimated from measurements as 1.45 and 0.98 $cm^2\ V^{-1}\ s^{-1}$, respectively. The electronic transport performance of MoS_2 based devices (FETs and photodetectors) are found to be unexpectedly better than the WS_2 based devices in terms of effective carrier mobility and photoresponsivity at ambient atmosphere and temperature. Our results suggest that WS_2 is more sensitive to ambient conditions in comparison to MoS_2, in spite of its theoretically estimated superior performance.

1 Introduction

Two dimensional (2D) materials era and the 2D material based electronics have begun with the exploration of the thinnest material, graphene in 2004 [1]. Graphene is the most studied 2D material because of its unique and exceptional mechanical, electrical and optical properties [2, 3]. However, the role of graphene in electronic applications has been limited due to its semi-metallic nature (having zero bandgap) which degrades the current ON/OFF performance of the fabricated electronic devices. 2D transition metal dichalcogenide (TMDCs) family is another widely studied group of 2D materials since the discovery of graphene. The presence of a direct bandgap due to the quantum confinement in 2D TMDCs makes them highly desirable for future electronic and optoelectronic device applications.

Both monolayer MoS_2 and WS_2 have received comparatively more attention because of their outstanding properties. They demonstrate wide direct bandgaps (1.8–2 eV) [4–6], strong photoluminescence (PL) emission [4, 7], thermal and mechanical stability [8] and large area growth ability [9]. According to the theoretical studies, MoS_2 and WS_2 based field effect transistors (FETs) have been estimated to have high current ON/OFF ratios as much as 10^9 and 10^6 and high effective carrier mobilities up to 340 and 1100 $cm^2\ V^{-1}\ s^{-1}$, respectively [10]. Experimental results on MoS_2 and WS_2 FETs also exhibit promising performances, even though they are underperforming compared to the theoretical results. The fabricated MoS_2 and WS_2 based transistors have been shown to operate with high effective carrier mobilities up to 217 and 60 $cm^2\ V^{-1}\ s^{-1}$, high current ON/OFF ratios of $\sim 10^8$ and $\sim 10^6$ and short channel immunity [11], respectively. The photo detection performance of these devices has also been measured as $\approx 10^4\ AW^{-1}$ with a response time of 10 s for MoS_2 based photodetectors and $\approx 10^{-3}\ AW^{-1}$ with a response time of several seconds for WS_2 based ones [12, 13].

✉ Feridun Ay
feridunay@anadolu.edu.tr

[1] Department of Electrical and Electronics Engineering, Anadolu University, Eskişehir 26555, Turkey

[2] Department of Materials Science and Engineering, Anadolu University, Eskişehir 26555, Turkey

[3] Department of Mechanical Engineering, Anadolu University, Eskişehir 26555, Turkey

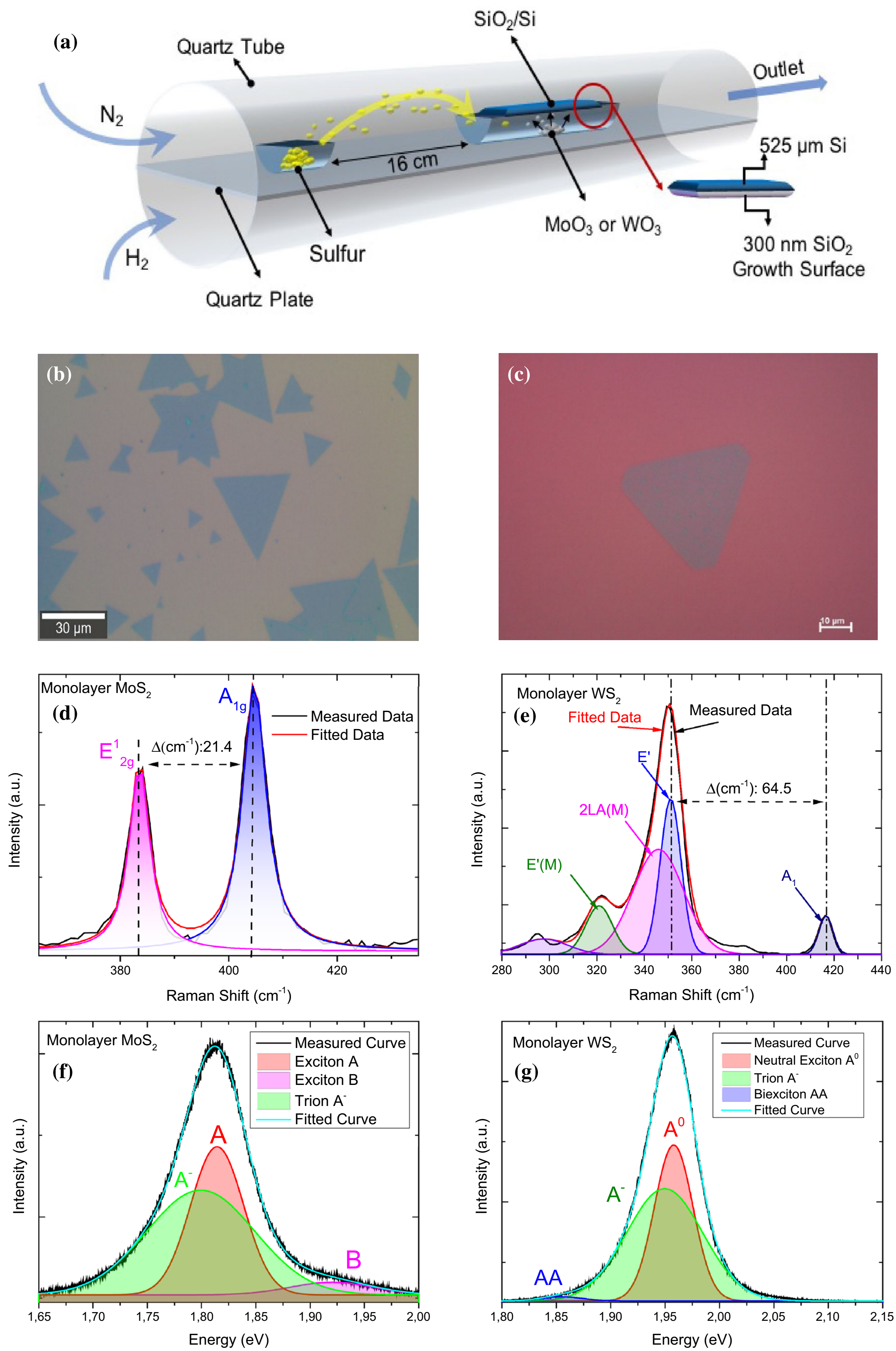
(a)
Quartz Tube
SiO2/Si
Outlet
N2
16 cm
525 µm Si
MoO3 or WO3
Sulfur
H2
300 nm SiO2
Growth Surface
Quartz Plate
(b)
30 µm
(c)
10 µm
Monolayer MoS2
(d)
A1g
E1 2g
Δ(cm-1):21.4
Measured Data
Fitted Data
Intensity (a.u.)
380
400
420
Raman Shift (cm-1)
Monolayer WS2
(e)
Fitted Data
Measured Data
E'
Δ(cm-1): 64.5
2LA(M)
E'(M)
A1
280
300
320
340
360
380
400
420
440
Raman Shift (cm-1)
Monolayer MoS2
(f)
Measured Curve
Exciton A
Exciton B
Trion A-
Fitted Curve
A
A-
B
1,65
1,70
1,75
1,80
1,85
1,90
1,95
2,00
Energy (eV)
Monolayer WS2
(g)
Measured Curve
Neutral Exciton A0
Trion A-
Biexciton AA
Fitted Curve
A0
A-
AA
1,80
1,85
1,90
1,95
2,00
2,05
2,10
2,15
Energy (eV)

◂**Fig. 1** **a** Schematic of the growth of CVD system for MoS_2 and WS_2. The optical images of **b** MoS_2 and **c** WS_2 flakes, Raman spectra with Lorentzian fits of **d** MoS_2 and **e** WS_2, PL spectrums with Gaussian fits of **f** MoS_2 and **g** WS_2

The mentioned FETs above have been fabricated from exfoliated MoS_2 and WS_2 flakes. On the other hand, the devices fabricated from chemical vapor deposition (CVD) grown flakes have been reported to have lower mobilities and lower current ON/OFF ratios between 0.1 to ≈ 50 $cm^2\ V^{-1}\ s^{-1}$ and ~ 10^3 to ~ 10^5 [14], respectively. The observed performance differences between CVD grown and exfoliated flakes are because of the differences between the crystal qualities and the defects induced during CVD process [15]. The exfoliated MoS_2 and WS_2 have high quality and low defect density but mechanical exfoliation is not a suitable method for industrial scale device fabrication and high-volume manufacturing. Therefore, the studies focusing on CVD grown devices are of crucial importance for future electronics and optoelectronics.

The performance difference between theoretical and experimental results is also due to the surface sensitivity of 2D materials. It is possible that their high surface to volume ratio enables physically adsorbed oxygen (O_2) and water (H_2O) molecules from ambient medium that serves as surface trapped states and affects their charge carrier transport properties [16]. As an evidence of this effect, Ahn et al. reported that the effective carrier mobility of MoS_2 based FETs increased four times when the sample is characterized under vacuum conditions [15]. Moreover, Lan et al. showed that the photoresponsivity of WS_2 based photodetectors is increased under vacuum or low humidity conditions [12]. As summarized above, since $MoS_2$and WS_2 are very important candidates for future electronic and optoelectronic devices, there have been numerous studies on MoS_2 and WS_2 individually. However, there are few studies focusing on comparative properties of WS_2 and MoS_2 under same growth and characterization conditions.

In this study, we report on the electronic transport and physical properties of MoS_2 and WS_2 based devices where their flakes are grown in the same CVD system, thus enabling a systematic comparison. Electronic transport properties of the fabricated FETs are characterized under the same ambient conditions to measure their relative performances. The electronic transport properties of the fabricated devices are examined comparatively in terms of field effective carrier mobility (μ_{FE}), current ON/OFF ratio and threshold voltages. The FETs of MoS_2 and WS_2 show reasonably high μ_{FE} of 1.45 and 0.98 $cm^2\ V^{-1}\ s^{-1}$, respectively. This indicates comparable electronic properties with exfoliated and CVD grown flake samples. In addition, the photo detecting performance of the fabricated devices is measured and compared.

2 Experimental details and characterization

2.1 MoS_2 and WS_2 synthesis

The CVD growth of 2D MoS_2 and WS_2 structures is performed in a home-built, dual-zone furnace with a 70 mm horizontal quartz tube at atmospheric pressure. Monolayer MoS_2 and WS_2 flakes are grown by using face-down substrate configuration as described by Ozden et al. [17]. The growth zone configuration of the set-up is depicted in Fig. 1.a. SiO_2/Si substrate is positioned face-down above the MoO_3 or WO_3 precursors. Quartz boats containing the precursors are placed on the quartz plate and therefore are positioned at the center of the quartz tube. Sulfur is placed at the upstream direction of the furnace having 16 cm distance with the metal-oxide precursors. The precursor amounts are kept constant for both MoS_2 and WS_2 growth processes at values of 150 mg for S and 1 mg for MoO_3 and WO_3, respectively. The growth procedure can be summarized as follows: 1 mg of MoO_3 (Sigma-Aldrich, 99.5%) and 150 mg of S (Sigma-Aldrich, 99.5%) powders are used as precursors and reacted to form MoS_2 flakes at 700 °C under 400 sccm N_2 flow. Similar to MoS_2 growth configuration, 1 mg of WO_3 (Sigma-Aldrich, 99.5%) and 150 mg of S powders have been used as precursors to form WS_2 flakes at 950 °C, under 95 sccm N_2 and 5 sccm H_2 on SiO_2/Si substrates. An inner one side-sealed quartz tube (2 cm diameter) is used to confine or keep WO_3 vapor on the substrate. The distance between Sulphur and oxide precursors is fixed to 16 cm.

The grown structures are analysed by using Witec Alpha 300 R μ-Raman and photoluminescence (PL) spectroscopy system with a Zeiss 50X microscope objective having a numerical aperture (NA) of 0.8. A 532 nm CW laser with 1 mW laser power and 0.2 s integration time was used for Raman spectra. The integration time used for the PL measurement was 0.03 s. The AFM measurements were done with Nanomagnetic-ezAFM system.

2.2 Device fabrication and characterization

Both WS_2 and MoS_2 triangular flake based devices are fabricated as back-gated FETs. The devices are fabricated on as-grown substrate without any transfer process to eliminate the transfer-originated effects. Source and drain electrodes are firstly patterned by optical lithography and 90 nm of Au is deposited on top of 10 nm Ti by thermal evaporation. After the fabrication process, all devices are baked on a hot plate for 10 min at 110 °C to remove any solvents introduced during the fabrication. Highly doped n-type 500 μm–thick silicon wafer (1–10 Ω cm) with

270 ± 35 nm SiO_2 dielectric layer is used as the back gate electrode and gate dielectric, respectively. The electronic transfer characteristics of the four fabricated MoS_2 and WS_2 devices are measured at room temperature under ambient conditions by a grounded home-built probe station with a Keysight B2902a source/measure unit.

3 Results and discussion

3.1 Surface morphology and optical characterization

Figure 1b, c show the optical microcopy images of MoS_2 and WS_2 flakes, respectively. In Fig. 1d, e Raman finger prints of MoS_2 (E^1_{2g} and A_{1g}) and WS_2 (E′(M), 2LA(M), E′ and A_1) have been identified and deconvoluted using Lorentzian curves to indicate the individual Raman modes [18, 19]. The layer numbers (thickness) of MoS_2 and WS_2 can be identified from Raman shift differences of E and A modes or exact Raman mode positions of materials. The E and A modes Raman shift differences are found to be 21.4 ± 0.1 and 64.5 ± 0.2 cm^{-1} and that indicate monolayer MoS_2 and WS_2, respectively [18].

Typical room temperature PL spectra of monolayer MoS_2 and WS_2 are shown in Fig. 1f, g where measurement is performed by using a 2.33 eV (532 nm) excitation wavelength laser at room temperature. The PL spectra of MoS_2 and WS_2 structures consist of three different radiative recombination mechanisms that are as attributed to exciton (A and B), trion (A^-) and biexciton (AA) [20, 21]. The measured PL spectra of materials are deconvoluted to three Gaussian curves which represent A (or B), A^- and AA. The centers of A-exciton, B-exciton and AA-trion which are represented in Fig. 1f have been extracted as 1.81, 1.92 and 1.79 eV for MoS_2, respectively. The intensity of A-exciton is very high with respect to the intensity of B-exciton, which is an indication of the monolayer MoS_2. In Fig. 1g the PL spectra of WS_2 with A^0-neutral exciton, A^--trion and AA-biexciton is shown. The centers of A^0, A^- and AA are at 1.96, 1.95 and 1.85 eV, respectively. Because of the excitation wavelength (2.33 eV) it is not possible to determine the B-exciton of WS_2 which lies around 2.4 eV [20].

The PL spectra of WS_2 and MoS_2 are very sensitive to doping levels or defect densities. In other words, the integrated intensity ratio of trion (I_X) to exciton (I_{X^-}) peaks gives information about the defect densities, which is due to the relationship between charge carrier density and quasi particle concentration that are based on mass action law [22–24].

In this manner, (I_{X^-}/I_X) has been extracted from over 500 fitted spectra and found to be 0.7 and 0.8 for MoS_2 and WS_2, respectively. MoS_2 and WS_2 are found to have similar defect densities.

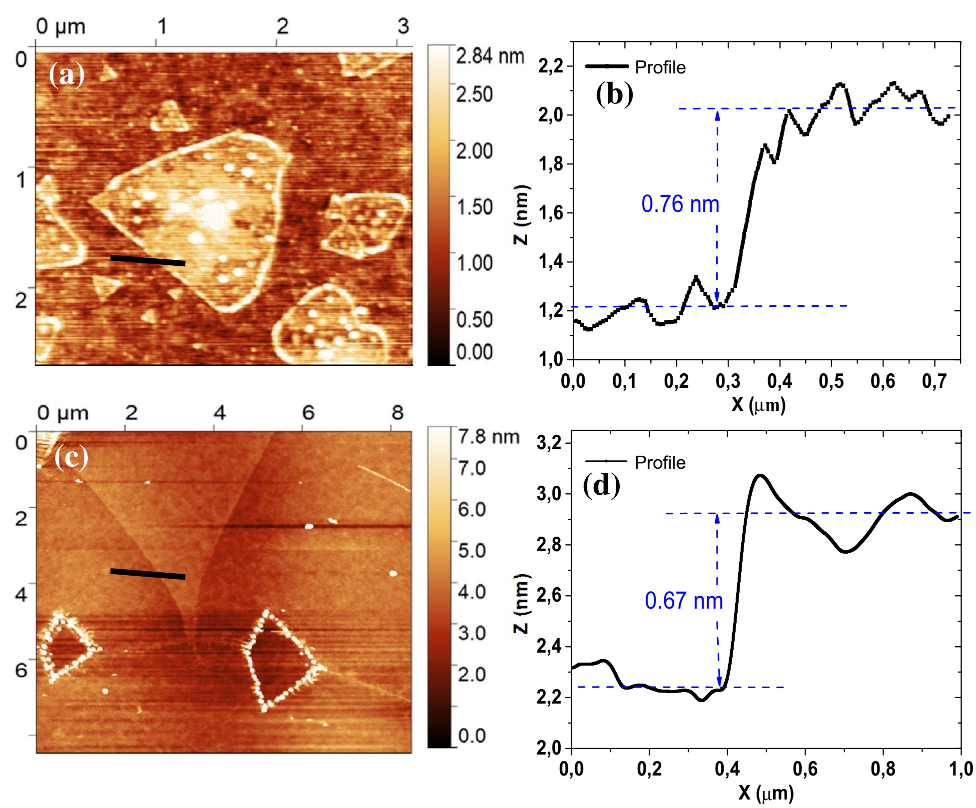

Fig. 2 **a** 3 µm × 3 µm AFM image of MoS_2 flakes and **b** the height profile of MoS_2 flake taken from black line on (**a**), **c** 8 µm × 8 µm AFM image of WS_2 flake and **d** the height profile from black line on AFM image (**c**)

Figure 2a shows 3 μm × 2.5 μm AFM image of MoS_2 triangles which indicate a maximum height of 2.4 nm caused by contamination. The step height profile of MoS_2 triangle is presented in Fig. 2b where the thickness of the flake is determined as one layer (0.76 nm). The 8 μm × 7 μm AFM image of WS_2 presented in Fig. 2c shows a uniform flake surface without any contamination. In Fig. 2d the structure of WS_2 flake is also determined as a monolayer (0.67 nm).

3.2 Electrical characterization

The cross-sectional diagram of the fabricated devices with electrical connections is demonstrated in Fig. 3a. FETs are fabricated on a 300 nm thick gate oxide layer on top of a highly doped 525 nm thick Si substrate. Gate bias is applied to the Si substrate to modulate our FETs. In order to make a meaningful comparison, both MoS_2 and WS_2 based devices are designed with the same active region channel length determined as L_{CH} = 4 μm. Electrical measurement of all the devices are conducted in ambient atmosphere, under dark and illuminated conditions at room temperature.

According to the measured transfer curves, MoS_2 and WS_2 based FETs display n-type behavior. The threshold voltages (V_{TH}) are determined from the linear regime of the on-state conduction. The tangent line with maximum slope to I_{DS}–V_{BG} curve at the peak transconductance (g_m) is linearly extrapolated to V_{BG} (axis) to extract V_{TH}. The extracted V_{TH} values of MoS_2 and WS_2 FETs are ~ 41 and ~ 124 V, respectively. According to transfer curves the devices have a low gate modulation efficiency. Field effect mobilities are calculated from estimated transconductance $g_m = \partial I_{DS}/\partial V_{BG}$ using:

$$\mu_{FE} = \frac{L_{CH}}{W_{CH}} \frac{1}{V_{DS}C_g} \frac{\partial I_{DS}}{\partial V_{BG}} \left(\mathrm{cm^2V^{-1}s^{-1}}\right) \tag{1}$$

where μ_{FE} is the field effective carrier mobility, I_{DS} is drain-source current, L_{CH}/W_{CH} is the ratio of channel length to channel width, V_{DS} is bias voltage and C_g is the gate capacitance per unit area $C_g = \varepsilon_g/t_g$. ε_g and t_g is the dielectric constant and the thickness of gate oxide, respectively. The FETs of MoS_2 and WS_2 show reasonably high μ_{FE} of 1.45 and 0.98 $cm^2\ V^{-1}\ s^{-1}$, indicating comparable electronic performance with previously reported CVD grown samples [15, 25]. Although the theoretical estimation addresses a higher mobility for WS_2 based devices, our MoS_2 based FETs show a better performance in terms of mobility.

The contact resistance effect is not accounted for mobility estimation which may result in degraded mobilities. A dedicated contact resistance measurement is expected to increase the value of field effect mobility around ten percent [26]. In addition to that, the gate voltage sweep modulates the number of carrier electron energy levels. These levels are filled at the electrode-active region intersection position which is the junction point. That modulation depends on capacitive coupling between the gate electrode and active region [21]. The efficiency of this capacitive coupling depends strongly on the quality of the gate oxide, in other words dielectric

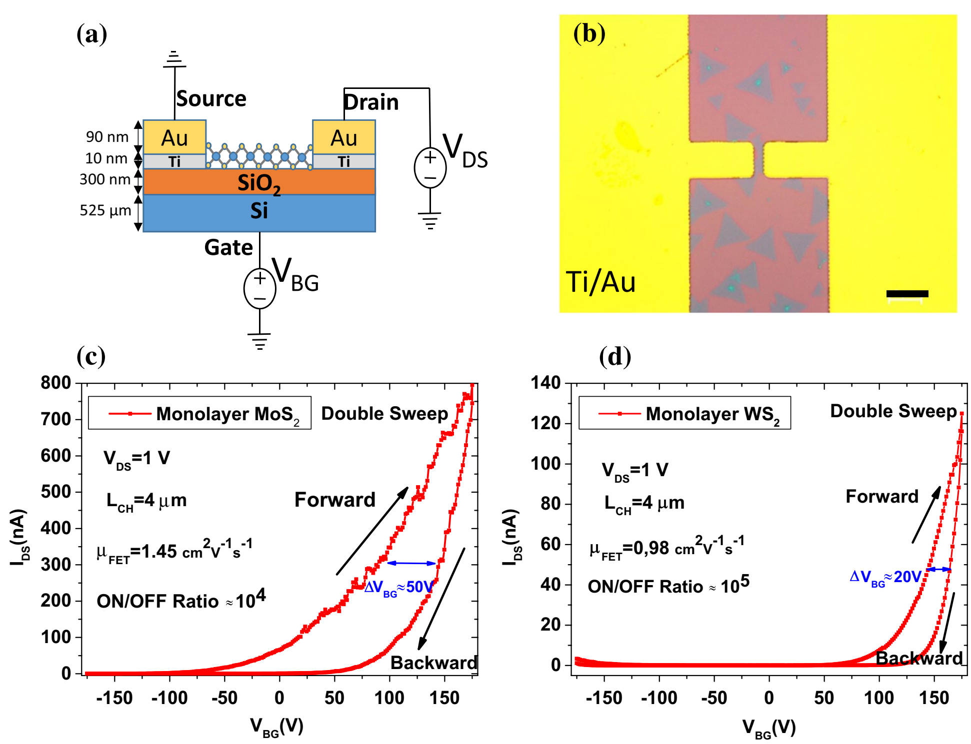

Fig. 3 **a** The cross-sectional view of the device structure, **b** the optical image of a typical device (scale 10 μm), the transfer curves (I_{DS}–V_{BG}) of **c** MoS_2 and **d** WS_2

constant of the gate oxide. Since the devices are fabricated on as-grown substrates to avoid any contamination from the transfer process, the substrates have been exposed to very high growth temperatures like 700 and 950 °C. These high temperatures may degrade the capacitive coupling efficiency of gate oxide by inducing defects during growth that may also cause degradation in effective carrier mobility and threshold voltages. The subthreshold swing (SS) values of MoS_2 and WS_2 devices are inferred to be comparatively high according to the ones reported in the literature, 19.59 V/decade and 14.66 V/decade, respectively [27]. Furthermore, the current ON/OFF ratios of devices are obtained as ~ 10^4 and ~ 10^5 for MoS_2 and WS_2, respectively. Both devices show rather high ON/OFF ratios performances.

Figure 4a, b represent the characteristic curves (I_{DS}–V_{DS}) of MoS_2 and WS_2 based devices when the gate modulation voltage changes from $V_{BG} = -20$ V to $V_{BG} = 175$ V with a step rate of 20 V. The V_{DS} voltage is swept from 0 to 3 V to show the operation regions of the FETs. The saturation region of both types of the devices can be defined as the region where $V_{GS} \geq V_{TH}$ and $V_{DS} \geq 0.5$ V. The linear region (ohmic region) is in the range $V_{GS} \geq V_{TH}$ and $0\text{ V} \leq V_{DS} \leq 0.5$ V. The maximum saturation currents (I_{DSS}) have been measured as 340 and 42 nA for MoS_2 and WS_2 FETs, respectively. Two device types show similar characteristic curve behaviors except that MoS_2 has a higher I_{DSS} current and WS_2 operates with a higher gate modulation response when device is in the saturated operation region.

3.3 Photoresponsivity

An important application area of 2D MoS_2 and WS_2 structures is optoelectronic where they are used as active layers of photodetectors, phototransistors and solar cells [12, 28, 29]. In Fig. 5a, b the photo-responsive characteristics of

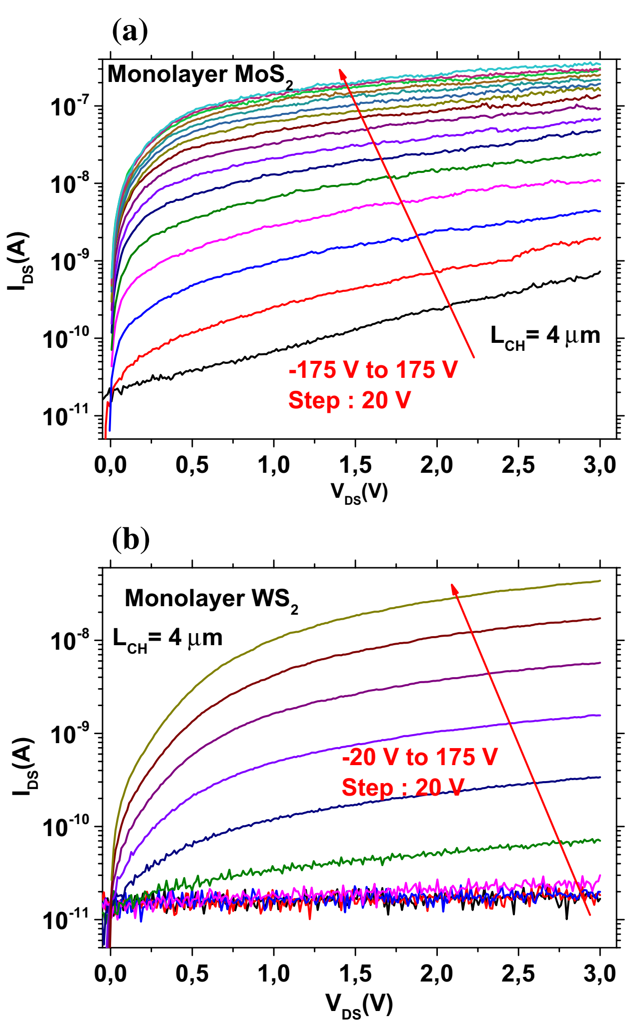

Fig. 4 The output characteristic curves (I_{DS}–V_{DS}) of **a** MoS_2 and **b** WS_2

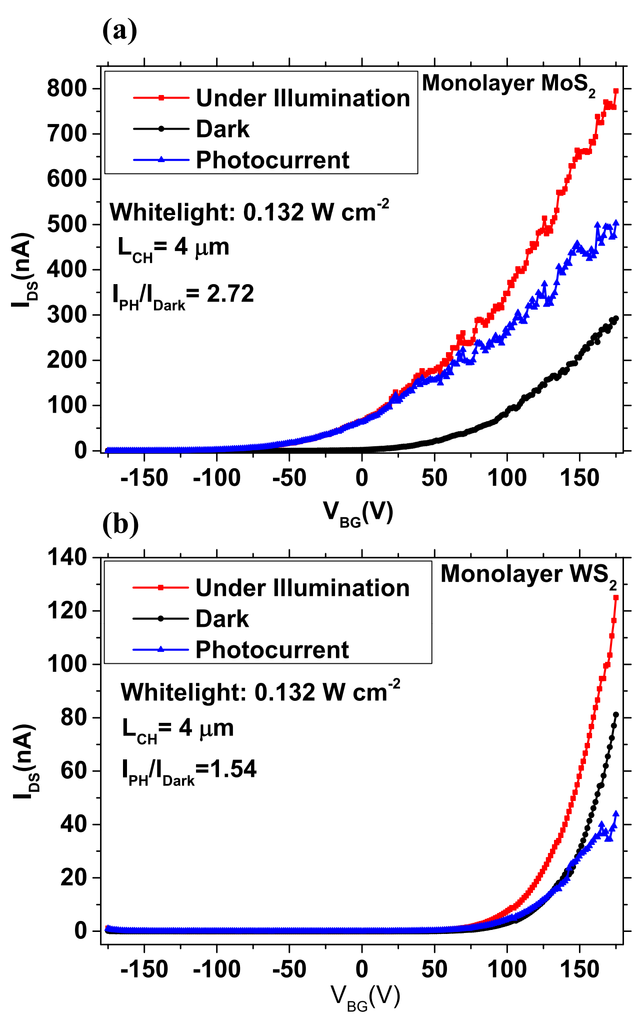

Fig. 5 The transfer curves (I_{DS}–V_{DS}) of **a** MoS_2 and **b** WS_2 under dark and illumination conditions with plotted photocurrent (I_{PH})

Table 1 The photodetector performance results of MoS_2 and WS_2 devices

	MoS_2	WS_2
Current ON/OFF ratio	~ 10^4	~ 10^5
Mobility μ_{FE} ($cm^2\ V^{-1}\ s^{-1}$)	~ 1.45	~ 0.98
Threshold voltage (V)	~ 41	~ 124
Hysteresis range (V)	~ 50	~ 20
Responsivity R (AW^{-1})	~ 14	~ 1.3

MoS_2 and WS_2 based devices under dark and illuminated conditions are presented.

A white light with an intensity of 0.132 W cm^{-2} has been used as illumination source. Photocurrent is defined as the difference between the current under illumination (I_{Il}) and the dark current (I_D) as in Eq. (2).

$$I_{PH} = I_{Il} - I_D\ (A) \tag{2}$$

As can be seen from Fig. 5, both devices are able to modulate the photocurrent according to the gate voltage. However, the modulation efficiency and maximum photocurrent of the MoS_2 based device is higher than that of WS_2 and can be originating from characterizing the devices under ambient conditions. Lan et al. reported that WS_2 is very sensitive to the measurement medium. They demonstrate a significant increase in photoresponsivity of WS_2 based photodetectors in vacuum with respect to measured samples in ambient atmosphere [12]. One can speculate that the surface sensitivity of WS_2 is higher than MoS_2.

As a second metric, ratio of maximum illuminated current to maximum dark current has been estimated as 2.72 and 1.54 for MoS_2 and WS_2, respectively, which again indicates that the MoS_2 based FETs have a higher sensitivity.

Another common benchmark in optical performance measurements is the responsivity (R) which is measured to evaluate the photodetector performance and it is defined as;

$$R = \frac{I_{PH}}{\emptyset}(AW^{-1}) \tag{3}$$

where I_{PH} is the photo current and Ø is irradiation intensity. The state of art responsivity values of 2D MoS_2 and WS_2 are between 1.1×10^{-3}–10^4 and 9.2×10^{-5}–1.88×10^{-2} AW^{-1}, respectively for visible irradiation [12, 13, 30–33]. The photoresponsivity of the devices are estimated to be considerably high according to state of the art as 14 and 1.3 AW^{-1} for MoS_2 and WS_2, respectively [34]. The photodetector performance results of the fabricated MoS_2 and WS_2 devices are summarized in Table 1.

4 Conclusion

In summary, we report on the transport and physical properties of monolayer MoS_2 and WS_2 based devices of which the active materials are grown in the same CVD system, fabricated with optical lithography and characterized under the same ambient conditions to understand their comparative performance. The back-gated, CVD grown MoS_2 based devices in ambient conditions without any encapsulation and doping process show higher effective carrier mobility, lower threshold voltage and higher photoresponsivity which are very important for high performance transistors and optoelectronic applications. On the other hand, WS_2 based devices which have the same configuration and measurement system as the MoS_2 based ones, exhibit high current ON/OFF ratio and low hysteresis behavior suggestively due to the lower density of the trap states between the dielectric material and WS_2 where this low hysteresis behavior is critical for electronic applications. Theoretical research studies estimate that WS_2 based FETs and photodetectors should present a superior performance. However, the photoresponsivity of the MoS_2 based devices (photodetectors) are unexpectedly found to be operating with a better performance than the WS_2 based devices at ambient atmosphere and temperature. The results suggest that MoS_2 based FET devices are more promising compared to WS_2 based ones under ambient conditions without any encapsulation, because 2D WS_2 structures are more sensitive to the ambient conditions with respect to 2D MoS_2 structures.

Acknowledgements This work was supported by Anadolu University Research Project Numbers: BAP1705F265, BAP1407F335 and BAP1605F424. A part of this work was supported by the BAGEP Award of the Science Academy.

References

1. K.S. Novoselov, A.K. Geim, S.V. Morozov, D. Jiang, Y. Zhang, S.V. Dubonos, I.V. Grigorieva, A.A. Firsov, Science **306**, 666–669 (2004)
2. K.S. Novoselov, V.I. Fal'ko, L. Colombo, P.R. Gellert, M.G. Schwab, K. Kim, Nature **490**, 192–200 (2012)
3. F. Akbar, M. Kolahdouz, S. Larimian, B. Radfar, H. Radamson, J. Mater. Sci. Mater. Electron. **26**, 4347–4379 (2015)
4. H.R. Gutierrez, N. Perea-Lopez, A.L. Elias, A. Berkdemir, B. Wang, R. Lv, F. Lopez-Urias, V.H. Crespi, H. Terrones, M. Terrones, Nano Lett. **13**, 3447–3454 (2013)
5. A. Özden, H. Şar, A. Yeltik, B. Madenoğlu, C. Sevik, F. Ay, N.K. Perkgöz, Phys. Status Solidi. (RRL) Rapid Res. Lett. **10**, 792–796 (2016)
6. M. Adelifard, R. Salamatizadeh, S. Ketabi, J. Mater. Sci. Mater. Electron. **27**, 5243–5250 (2016)
7. X. Li, H. Zhu, J. Materiom **1**, 33–44 (2015)
8. W. Brainard, NASA Tech. **Note TN D5141**, 1–22 (1969)

9. P.D. Cunningham, K.M. McCreary, A.T. Hanbicki, M. Currie, B.T. Jonker, L.M. Hayden, J. Phys. Chem. C **120**, 5819–5826 (2016)
10. W. Zhang, Z. Huang, W. Zhang, Y. Li, Nano Res. **7** 1731–1737 (2014)
11. B. Radisavljevic, A. Radenovic, J. Brivio, V. Giacometti, A. Kis, Nat Nanotechnol. **6**, 147–150 (2011)
12. C. Lan, C. Li, Y. Yin, Y. Liu, Nanoscale **7**, 5974–5980 (2015)
13. D. Kufer, G. Konstantatos, Nano Lett **15**, 7307–7313 (2015)
14. F.K. Perkins, A.L. Friedman, E. Cobas, P. Campbell, G. Jernigan, B.T. Jonker, Nano Lett. **13**, 668–673 (2013)
15. J.-H. Ahn, W.M. Parkin, C.H. Naylor, A.C. Johnson, M. Drndić, Sci. Rep. **7**, 4075 (2017)
16. C. Cong, J. Shang, X. Wu, B. Cao, N. Peimyoo, C. Qiu, L. Sun, T. Yu, Adv. Opt. Mater. **2**, 131–136 (2014)
17. A. Özden, F. Ay, C. Sevik, N.K. Perkgöz, Jpn. J. Appl. Phys. **56**, 06GG05 (2017)
18. W. Shi, M.-L. Lin, Q.-H. Tan, X.-F. Qiao, J. Zhang, P.-H. Tan, 2D Mater. **3**, 025016 (2016)
19. H. Li, Q. Zhang, C.C.R. Yap, B.K. Tay, T.H.T. Edwin, A. Olivier, D. Baillargeat, Adv. Funct. Mater. **22**, 1385–1390 (2012)
20. B. Zhu, X. Chen, X. Cui, Sci. Rep. **5**, 9218 (2015)
21. M. Chhowalla, D. Jena, H. Zhang, Nat. Rev. Mater. **1**, 16052 (2016)
22. Y. Fan, Y. Zhou, X. Wang, H. Tan, Y. Rong, J.H. Warner, Adv. Opt. Mater. **4**, 1573–1581 (2016)
23. N. Peimyoo, W. Yang, J. Shang, X. Shen, Y. Wang, T. Yu, ACS Nano **8**, 11320–11329 (2014)
24. S. Mouri, Y. Miyauchi, K. Matsuda, Nano Lett **13**, 5944–5948 (2013)
25. M. Amani, M.L. Chin, A.G. Birdwell, T.P. O'Regan, S. Najmaei, Z. Liu, P.M. Ajayan, J. Lou, M. Dubey, Appl. Phys. Lett. **102**, 193107 (2013)
26. F. Giannazzo, G. Fisichella, A. Piazza, S. Di Franco, G. Greco, S. Agnello, F. Roccaforte, Beilstein J Nanotechnol **8**, 254 (2017)
27. A. Nourbakhsh, A. Zubair, S. Joglekar, M. Dresselhaus, T. Palacios, Nanoscale **9**, 6122–6127 (2017)
28. F. Gong, W. Luo, J. Wang, P. Wang, H. Fang, D. Zheng, N. Guo, J. Wang, M. Luo, J.C. Ho, Adv. Funct. Mater. **26**, 6084–6090 (2016)
29. H. Tian, M.L. Chin, S. Najmaei, Q. Guo, F. Xia, H. Wang, M. Dubey, Nano Res. **9**, 1543–1560 (2016)
30. N. Perea-López, A.L. Elías, A. Berkdemir, A. Castro-Beltran, H.R. Gutiérrez, S. Feng, R. Lv, T. Hayashi, F. López-Urías, S. Ghosh, Adv. Funct. Mater. **23**, 5511–5517 (2013)
31. W. Zhang, J.K. Huang, C.H. Chen, Y.H. Chang, Y.J. Cheng, L.J. Li, Adv. Mater. **25**, 3456–3461 (2013)
32. N. Perea-López, Z. Lin, N.R. Pradhan, A. Iñiguez-Rábago, A.L. Elías, A. McCreary, J. Lou, P.M. Ajayan, H. Terrones, L. Balicas, 2D Mater. **1**, 011004 (2014)
33. C. Xie, C. Mak, X. Tao, F. Yan, Adv. Funct. Mater. **27**, 1603886 (2017)
34. L. Zeng, L. Tao, C. Tang, B. Zhou, H. Long, Y. Chai, S.P. Lau, Y.H. Tsang, Sci. Rep. **6** (2016)